Remote Sensing of Environment 237 (2020) 111519

Contents lists available at ScienceDirect

Remote Sensing of Environment

journal homepage: www.elsevier.com/locate/rse

A new method to retrieve the diurnal variability of planetary boundary layer height from lidar under different thermodynamic stability conditions

Tianning Su[a], Zhanqing Li[a,*], Ralph Kahn[b]

[a] Department of Atmospheric and Oceanic Science & ESSIC, University of Maryland, College Park, MD, 20740, USA
[b] Climate and Radiation Laboratory, Earth Science Division, NASA Goddard Space Flight Center, Greenbelt, MD, USA

ARTICLE INFO

Keywords:
Planetary boundary layer height
Thermodynamic stability
Lidar
Aerosols

ABSTRACT

The planetary boundary layer height (PBLH) is an important parameter for understanding the accumulation of pollutants and the dynamics of the lower atmosphere. Lidar has been used for tracking the evolution of PBLH by using aerosol backscatter as a tracer, assuming aerosol is generally well-mixed in the PBL; however, the validity of this assumption actually varies with atmospheric stability. This is demonstrated here for stable boundary layers (SBL), neutral boundary layers (NBL), and convective boundary layers (CBL) using an 8-year dataset of micropulse lidar (MPL) and radiosonde (RS) measurements at the ARM Southern Great Plains, and MPL at the GSFC site. Due to weak thermal convection and complex aerosol stratification, traditional gradient and wavelet methods can have difficulty capturing the diurnal PBLH variations in the morning and forenoon, as well as under stable conditions generally. A new method is developed that combines lidar-measured aerosol backscatter with a stability dependent model of PBLH temporal variation (DTDS). The latter helps "recalibrate" the PBLH in the presence of a residual aerosol layer that does not change in harmony with PBL diurnal variation. The hybrid method offers significantly improved PBLH detection, with better correlation and smaller biases, under most thermodynamic conditions, especially for SBL and CBL. Relying on the physical process of PBL diurnal development, different schemes are developed for growing, maintenance, and decaying periods. Comprehensive evaluation of this new method shows much better tracking of diurnal PBLH variation and significantly smaller biases under various pollution levels.

1. Introduction

The planetary boundary layer (PBL) is the lowest layer of the atmosphere, and tends to be relatively well-mixed (Garratt, 1994; Kaimal and Finnigan, 1994). It plays a dominant role in the surface-atmosphere exchanges of heat, moisture, momentum, gases, and pollutants (Caughey, 1984; Holtslag and Nieuwstadt, 1986; Mahrt, 1999). The PBL height (PBLH) is a meteorological variable that strongly affects the vertical extent of near-surface transport and dispersion processes, and is a key parameter in weather and climate modeling (Haeffelin et al., 2012; Seibert et al., 2000). As PBLH determines the volume available for near-surface pollutant dispersion, it is a crucial variable for monitoring and simulating surface pollutant behaviors (Gan et al., 2011; Monks et al., 2009; Su et al., 2018). Thermodynamic stability is a key property of the PBL; it influences convection, precipitation, and turbulence (Emanuel, 1994; Guo et al., 2017; Lilly, 1968; Matsui et al., 2004; Lou et al., 2019). Based on the thermodynamic stability in the lower atmosphere, the PBL can be classified into three dominant types: stable boundary layers (SBL), neutral boundary layers (NBL), and convective boundary layers (CBL) (Caughey and Palmer, 1979; Garratt, 1994; Liu and Liang, 2010).

Multiple approaches have been developed to determine the PBLH based on observations, including *in situ* radiosonde (Stull, 1988) and remote sensing (Menut et al., 1999) methods, as well as parameterizations based on laboratory experiments (Park et al., 2001). The most common approach for deriving PBLH is from radiosonde measurements (RS) of temperature, humidity, and/or wind profiles as a function of pressure (Angevine et al., 1994; Guo et al., 2016; Liu and Liang, 2010; Seidel et al., 2010; Zhang et al., 2018). Although RS is the traditional and standard method for determining PBLH, it has very limited coverage in both space and time. Regular RS launches occur routinely twice a day from a fixed set of meteorological stations, and thus cannot capture well the diurnal or spatial PBLH variations. Ground-based lidar, such as micropulse lidar (MPL), measures aerosol backscatter with high temporal and vertical resolutions, and has also been widely used to derive PBLH. (Eresmaa et al., 2006; Hageli et al.,

* Corresponding author. Department of Atmospheric and Oceanic Science & ESSIC, University of Maryland, College Park, MD, 20740, USA.
E-mail address: zhanqing@umd.edu (Z. Li).

https://doi.org/10.1016/j.rse.2019.111519
Received 9 February 2019; Received in revised form 21 June 2019; Accepted 2 November 2019

2000; Liu et al., 2018; Luo et al., 2014; Sawyer and Li, 2013; Su et al., 2017a; Tucker et al., 2009; Yang et al., 2013; Chu et al., 2019; Welton et al., 2000; Morille et al., 2007). Although the spatial coverage is still limited, several projects led by NASA and the Department of Energy offer ample MPL measurements, such as MPLNET, Atmospheric Radiation Measurement (ARM), DISCOVER-AQ, etc. (Campbell et al., 2002; Welton et al., 2001, 2002; Lewis et al., 2013; Crawford and Pickering. 2014). Numerous methods have been proposed to retrieve the PBLH from lidar, ranging from visual inspection (Boers et al., 1984), to setting a signal threshold (Melfi et al., 1985), wavelet transform (Cohn and Angevine, 2000; Davis et al., 2000), fitting to idealized profile (Steyn et al., 1999), changes in depolarization ratio (Bravo-Aranda et al., 2017), identifying maximum signal variance (Hooper and Eloranta, 1986; Su et al., 2017b; Zhang et al., 2016), and first (Flamant et al., 1997), logarithmic (Summa et al., 2013), normalized (He et al., 2006), and cubic root (Yang et al., 2017) gradient methods, as well as the combination of the wavelet technique and image processing (Lewis et al., 2013).

Although numerous algorithms have been applied to long-term PBL measurements, and have been validated at multiple sites over the world, most PBLH algorithms are designed for CBL conditions (e.g. Li et al., 2017a; Poltera et al., 2017). The afternoon PBL is typically considered convective, with a peak at ~15:00 local time; in contrast, SBL generally dominates at night (Nieuwstadt, 1984; Poulos et al., 2002). In addition, SBLs and NBLs can form under certain meteorological conditions during the day as well, and can occur even in the afternoon (Medeiros et al., 2005; Poulos et al., 2002; Stull, 1988; Zhang et al., 2018). Evaluation of these algorithms for SBLs has been limited, and in particular, evaluation of lidar-based PBL detection under the full range of atmospheric stability conditions is still lacking.

As such, the current study presents a new method to retrieve PBL variability from MPL under Different Thermo-Dynamic Stabilities (namely, the DTDS algorithm). The thermodynamic stability is represented by the near-surface potential temperature profile in the context of the boundary layer vertical structure. Long-term MPL measurements from 2010 to 2018, acquired at the Department of Energy's Atmospheric Radiation Measurement Southern Great Plains (ARM SGP) site, are used for validation. PBLH retrievals derived from the DTDS are compared with the commonly used gradient and wavelet methods, and are explicitly compared against RS results under SBL, NBL, and CBL conditions. The performance of PBLH derived from MPL under different aerosol loadings is also considered.

This paper proceeds as follows: Section 2 describes the study sites and MPL system. Section 3 describes the method in terms of its physical principles, implementation, and determination of the thresholds required by the DTDS method. Evaluation is presented in section 4, and a brief discussion and conclusion are given in Section 5.

2. Description of the site and instruments

2.1. Radiosonde

RS launches took place at least four times per day at the SGP site near Ponca City, Oklahoma (36°36′ N, 97°29′ W), usually at 00:30, 6:30, 12:30, and 18:30 local time (LT). To avoid inconsistency between summer and winter, daylight saving time (summer time) is used consistently for local time throughout the year. Besides the routine measurements at these fixed times, there are fewer, but still considerable, numbers of RS measurements acquired at other times of day, especially during special field experiments. Supplemental RS sampling at 0930, 1200, 1300, 1530, 1900 LT were acquired for around 4% of the total cases. In this study, we only utilize the RS data during 06:30–19:00 LT. RS vertical resolution varies according to the balloon ascent rate, but data points occur approximately 10 m apart. We resample the radiosonde data using linear interpolation to achieve a vertical resolution of 5-hPa.

We use a well-established method developed by Liu and Liang (2010) to retrieve the PBLH based on the gradient profile of potential temperature. Here, we focus only on PBL driven by buoyancy, and hence, low-level jet conditions are excluded, based on radiosonde wind profiles (Liu and Liang, 2010; Miao et al., 2018). Furthermore, the PBLH can be classified as SBL, NBL, or CBL based on the thermodynamic stability conditions. PBL types are determined by calculating the near-surface potential temperature difference (PTD) between the lowest fifth and second layers above the surface (i.e., an interval of 5-hPa). Specifically, if the PTD is higher than 0.1 K and the bulk Richardson number in the lowest 0.1 km is positive, the PBL is identified as SBL; if the PTD is between −0.1 K and 0.1 K, the PBL is identified as NBL; other PBL cases are considered CBL (Tokinaga et al., 2006; Zhang et al., 2018).

2.2. Micropulse lidar system

This study uses an MPL backscatter time series collected at the SGP site (36°36′ N, 97°29′ W). The dataset spans June 2010 through June 2018 with high continuity (Campbell et al., 2002). The MPL observed at 532 nm wavelength with both parallel and perpendicular polarization. The backscatter profiles have a vertical resolution of 15 m and a temporal resolution of 10 s. Due to incomplete laser pulses, there is a 150 m near-surface “blind zone”. As standard processes, background subtraction, saturation, overlap, after-pulse, and range corrections are applied to the raw MPL data to derive the normalized signal (NS) (Campbell et al. 2002, 2003; Yan et al., 2014). There are quality-control flags along with the MPL measurements. Erroneous data and rainy cases are eliminated from our analysis. We supplement these data with the MPL observations at the GSFC site (38 °59′ N, 76°50′ W) from MPLNET, following similar data processing procedures (Welton et al., 2001, 2002). We also collect RS data at a nearby NOAA station (USM00072403, 38 °59′ N, 77°29′ W) to match with MPL data at GSFC. MPL data and RS measurements during morning (0800LT) and afternoon are both available on 80 days between 2002 and 2016. Hereafter, “afternoon” refers to the period from 1200 to 1830 LT.

3. Development of the DTDS

3.1. A brief overview of existing algorithms

Numerous methods have been proposed to retrieve the PBLH from backscatter lidar. These methods rely on the principle that a temperature inversion often exists at the top of the PBL, trapping moisture and aerosols (Seibert et al., 2000), which causes a sharp decrease in the aerosol backscatter signal from the PBL upper boundary to the free troposphere. Traditionally, the methods fall into two categories: (i) gradient-based algorithms that track gradients in the vertical distribution of aerosols (i.e., gradients of the backscatter profiles (Flamant et al., 1997; He et al., 2006; Sicard et al., 2006; Summa et al., 2013; Yang et al., 2017), and (ii) wavelet transform algorithms that track the covariance transform of the Haar function (Baars et al., 2008; Brooks, 2003; Cohn and Angevine, 2000; Davis et al., 2000). The merits and limitations of these approaches were evaluated by Sawyer and Li (2013), who proposed a joint approach that takes advantage of the two, and can be applied to any type of measurements, including RS and lidar, and compared their performance.

In this paper, we compare the performance of the DTDS with the traditional algorithms over the diurnal range of stability conditions. The gradient method is adapted from Amiridis et al. (2007) and Flamant et al. (1997), and we set the first derivative of lidar backscatter signals as the gradient profile. The wavelet method is another commonly used, though more sophisticated, method. As a way of detecting step changes, the wavelet method was introduced by Gamage and Hagelberg (1993). The Haar wavelet can be defined as

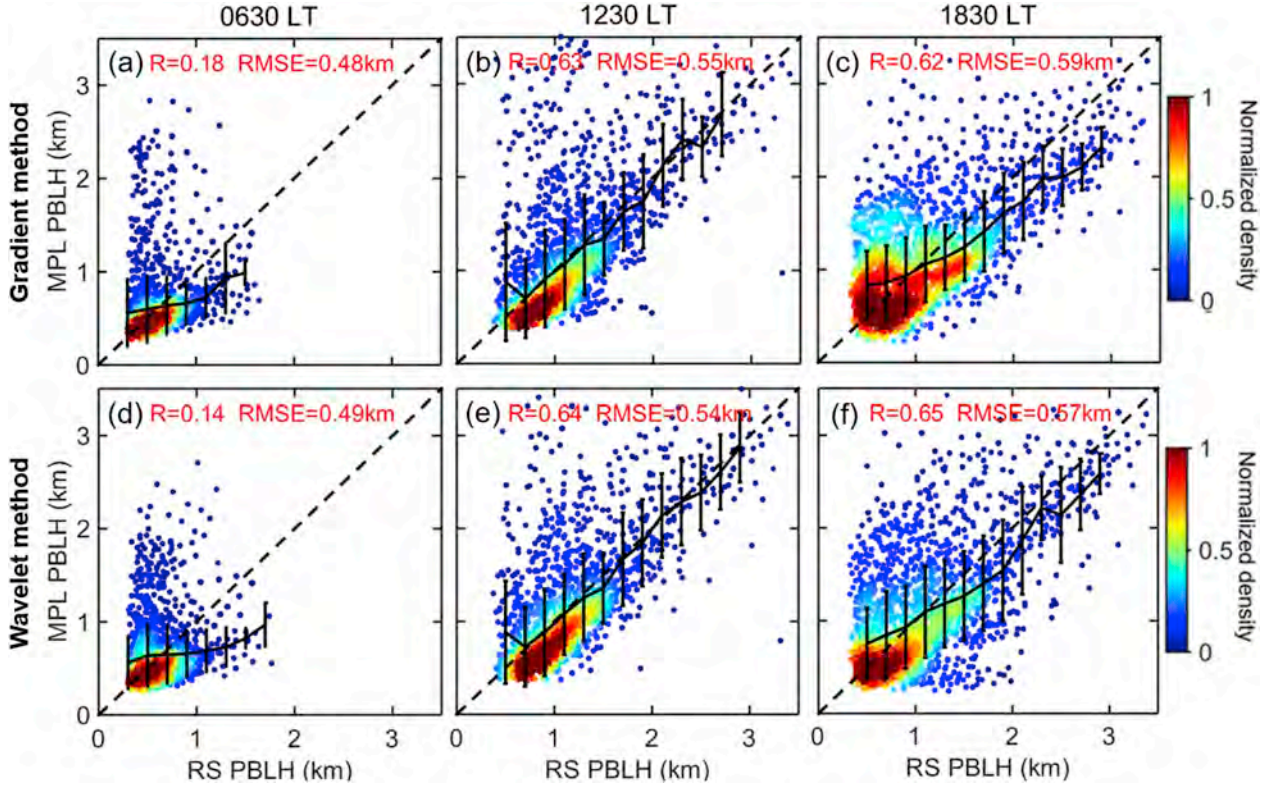

Fig. 1. Comparisons between MPL PBLH (derived by the gradient method) and RS PBLH for (a) 0630 LT, (b) 1230 LT, and (c) 1830 LT. Comparisons between MPL PBLH (derived by the wavelet method) and RS PBLH for (d) 0630 LT, (e) 1230 LT, and (f) 1830 LT. Correlation coefficients (R) and RMSE (root-mean-square error) are given in each panel.

$$\mathrm{h}\left(\frac{z-b}{a}\right)=\begin{cases}+1: & b-\frac{a}{2}\le z<b\\ -1: & b<z\le b+\frac{a}{2}\\ 0: & \textit{elsewhere}\end{cases} \tag{1}$$

where z is altitude, b translates the location where the function is centered, and a is called the "dilation" of the function. Then, the covariance transform of the Haar function $W_f(a, b)$ is defined as

$$W_f(a,b)=\frac{1}{a}\int_{z_b}^{z_t} f(z)\mathrm{h}\left(\frac{z-b}{a}\right)dz \tag{2}$$

where $f(z)$ is the lidar backscatter signal and z_t/z_b indicates the lower/upper limits of the profile, respectively. The value b at which $W_f(a, b)$ reaches its maximum value with a coherent scale of a is usually considered as the PBLH (Brooks, 2003). In this study, we select the dilation a as 400 m, which is consistent with previous studies (Compton et al., 2013; Davis et al., 2000).

In Fig. 1, we compare the PBLH derived from MPL using these two methods with RS results, for different local times (LT). There is generally much better agreement between MPL-PBLH and RS-PBLH at 1230 and 1830 LT than at 0630. This is clearly denoted by the distinct differences, factors of 3–4, in their linear correlation coefficients. The very poor agreement for morning cases is associated with the fact that the PBL is not well developed, as indicated by the existence of a strong surface inversion and residual layers. All these factors complicate PBLH identification. As such, these MPL methods fail in identifying the PBLH under the SBL conditions that tend to dominate in the morning.

Despite the dominance of the CBL in the afternoon, SBL and NBL can also occur under some meteorological conditions. Based on the RS data from SGP, SBL dominates during the morning (0630LT), and its occurrence frequency is more than 90% in the dataset used for the current study. In the noontime (1230LT), the occurrence frequency of CBL is only ~3%, followed by 43% for NBL, and 54% for SBL. In the late afternoon (1830LT), the SBL frequency is about 38%, followed by 47% for NBL, and 15% for CBL. Fig. 2 shows a comparison of afternoon PBLH derived from MPL and RS under SBL, NBL, and CBL conditions. In the afternoon (1200–1830 LT), SBL, NBL and CBL conditions occur for 19%, 45%, and 36% of total cases in our dataset. Again, MPL-PBLH shows much better agreement with RS-PBLH for CBL and NBL conditions than for SBL, especially where RS-PBLH < 1.0 km. Therefore, MPL has a major problem retrieving PBLH for weak convective as well as SBL cases. Note also that for all three PBL types, root-mean-square error (RMSE) values are around 0.6 km.

3.2. Description of the DTDS

In order to overcome problems with SBL conditions, we develop a new approach for retrieving MPL-PBLH that performs better and more uniformly under all thermodynamic stability conditions. The physical basis of our DTDS method is to account for both the vertical coherence and temporal continuity of the PBLH. Given that the aerosol within the boundary layer is usually well mixed, a distinct step due to aerosol is sought in the backscatter signal as the top of a PBL, which follows the gradient and wavelet transform methods. The development of the PBL can be divided into three phases: growing, decaying, and "other" (i.e., maintenance), and different selection schemes can be applied to these different phases. A schematic diagram of the DTDS is presented in Fig. 3, and the procedures are detailed below.

First, the MPL backscatter profiles are averaged over 10-min intervals. Then, we identify the local maximum positions (LMPs) (range: 0.25–4 km) in the covariance transform function collocated with a signal gradient larger than a certain threshold. The threshold values are discussed in Section 3.3. The aerosol vertical structure can be represented by multiple LMPs. Each LMP is the potential position of PBLH.

$H(i)$ represents the retrieved PBLH for time i. For the starting point

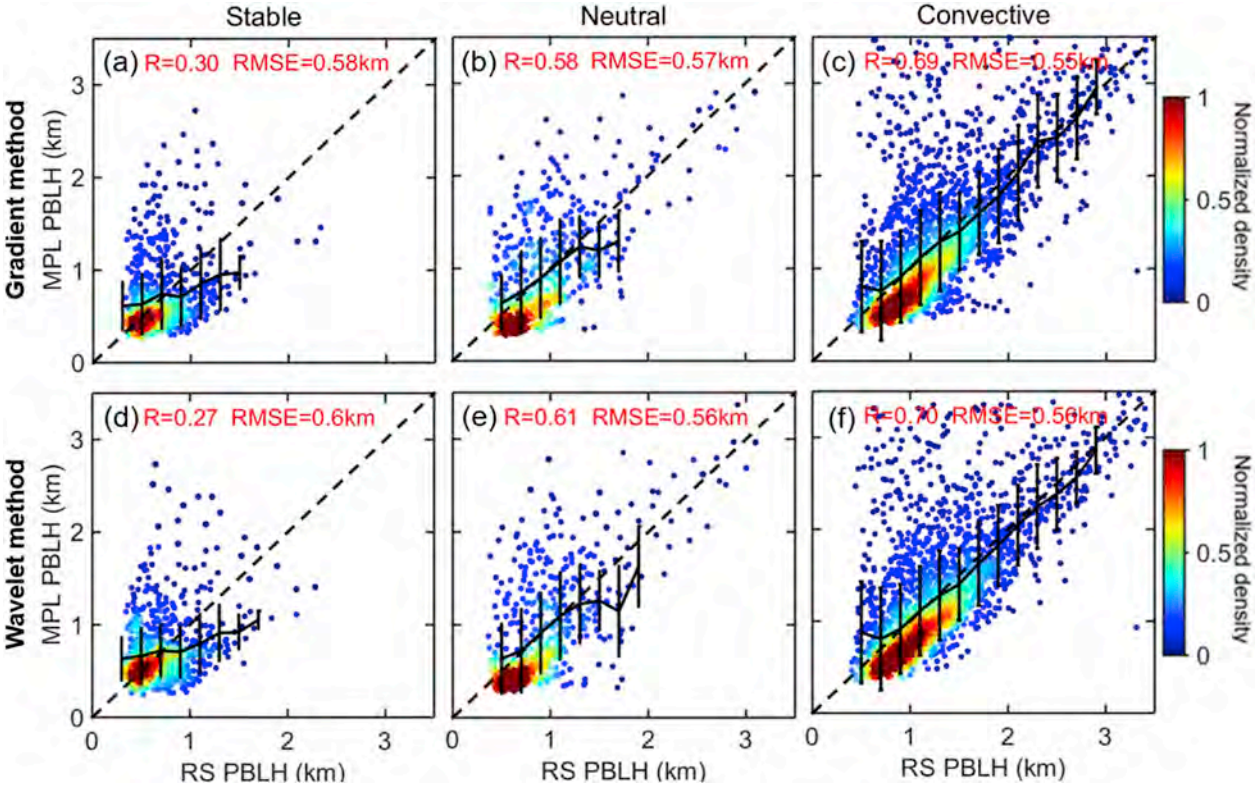

Fig. 2. Comparisons between MPL PBLH (derived by the gradient method) and RS PBLH for (a) stable (SBL), (b) neutral (NBL), and (c) convective (CBL) boundary layers during afternoon (1200–1900 LT). Comparisons between MPL PBLH (derived by the wavelet method) and RS PBLH for (d) SBL, (e) NBL, and (f) CBL.

(0700 LT), the PBLH ($H(0)$) is given by the morning RS launched at 0630 LT (or the lowest LMP if RS is not available), after which we select the closest LMP at 0710 to $H(0)$ as $H(1)$. If we find a suitable $H(1)$, we identify the closest LMP at the next timestep as $H(2)$. Generally, for time i+1, we select the closest LMP to $H(i)$ as $H(i+1)$. The maximum variation rate (*Max*) is set to 0.2 km, so the difference between $H(i+1)$ and $H(i)$ needs to be smaller than *Max*. Otherwise, $H(i+1)$ is set to equal to $H(i)$, and is called a "quasi retrieval". If we obtain two consecutive quasi retrievals, $H(i)$ and $H(i+1)$, we set $H(i+1)$ to the lowest LMP in time i+1, and then, determine $H(i+2)$ using above mentioned algorithms.

As shown in Fig. 3b, the selection scheme is different for the growing (0830–1400) and decaying (1630–1900) PBL phases, defined by these pre-selected local time periods. Due to surface heating by solar radiance, the PBLH tends to rise quickly during the growing period, and generally reaches its daily maximum monotonically. For time i+1, if we find two LMPs adjacent to the previous $H(i)$, we preferentially select the one higher than $H(i)$ as $H(i+1)$ during this period. However, we preferentially select the one lower than $H(i)$ as $H(i+1)$ during the decaying period. Details of the selection scheme for different periods are shown in Fig. 3b. Generally, during the growing phase, we favor the nearest LMP above *H(i)* as *H(i+1)*. However, if the two nearest LMPs during the growing phase are above and below *H(i)* and the upper LMP is twice as far from *H(i)* as the lower, we will still select the lower one as *H(i+1)*. We implement a similar selection scheme for the decay phase, but in just the opposite sense to that of the grow phase. If we cannot find two LMPs adjacent to *H(i),* the potential PBLH position is selected as the nearest LMP.

A restart mechanism is included in this algorithm, controlled by the parameter "*Re*," which remains at 0 as long as the selection scheme in Fig. 3b is successful. For two contiguous times (i and i+1), if we cannot find the suitable $H(i)$ and $H(i+1)$, *Re* becomes larger than 1, and the algorithm "restarts." Specifically, the lowest LMP at time i+2 is selected as $H(i+2)$, and the iterative process is restarted from there.

Cloud inevitably causes a step signal in the lidar backscatter, and thus, affects the PBLH retrievals. Depending on type, clouds can interfere with PBLH retrievals, though boundary layer top clouds can also be regarded as defining the PBLH. During the development of the PBLH over land, fair-weather cumulus are often generated from convection and high-humidity located at the top of PBL. Following the threshold method, cloud or aerosol layers can be detected based on the gradient of range-corrected signals (Dupont et al., 2011; Platt et al., 1994). Cloud can be further distinguished based on the values of *T* and *D* for a certain layer, where *T* represents the ratio of the peak signal to that of the layer base and *D* represents the maximum negative slope within this layer. When $T > 3$ or $D < -7$, the layers are classified as clouds (Wang and Sassen, 2001; Zhao et al., 2014). All low-level clouds below 4 km are identified, and then, we label these clouds as "boundary layer clouds" if their tops coincide with the previous PBLH value retrieved under cloud-free conditions to within 0.35 km. Due to the frequent occurrence of convection, we only identify boundary layer clouds during the growing and maintenance periods. Other low-level cloudy cases are excluded from the analysis.

3.3. Sensitivity test of thresholds

The detection of LMPs is a crucial part of the DTDS, and an appropriate threshold is needed to identify step signals in the gradient profiles. The method is quite sensitive to the threshold selection. A low threshold value will lead to too many LMPs, which complicates PBLH identification, whereas too high a threshold value will constrain the LMP selection, which could filter out the actual PBLH. Therefore, we conducted a sensitivity test to select the threshold.

In many studies, the threshold for detecting step signals in PBL lidar profiles is set to a constant value (Hageli et al., 2000; Yang et al., 2013). Instead, we apply a dynamic threshold, which is associated with the

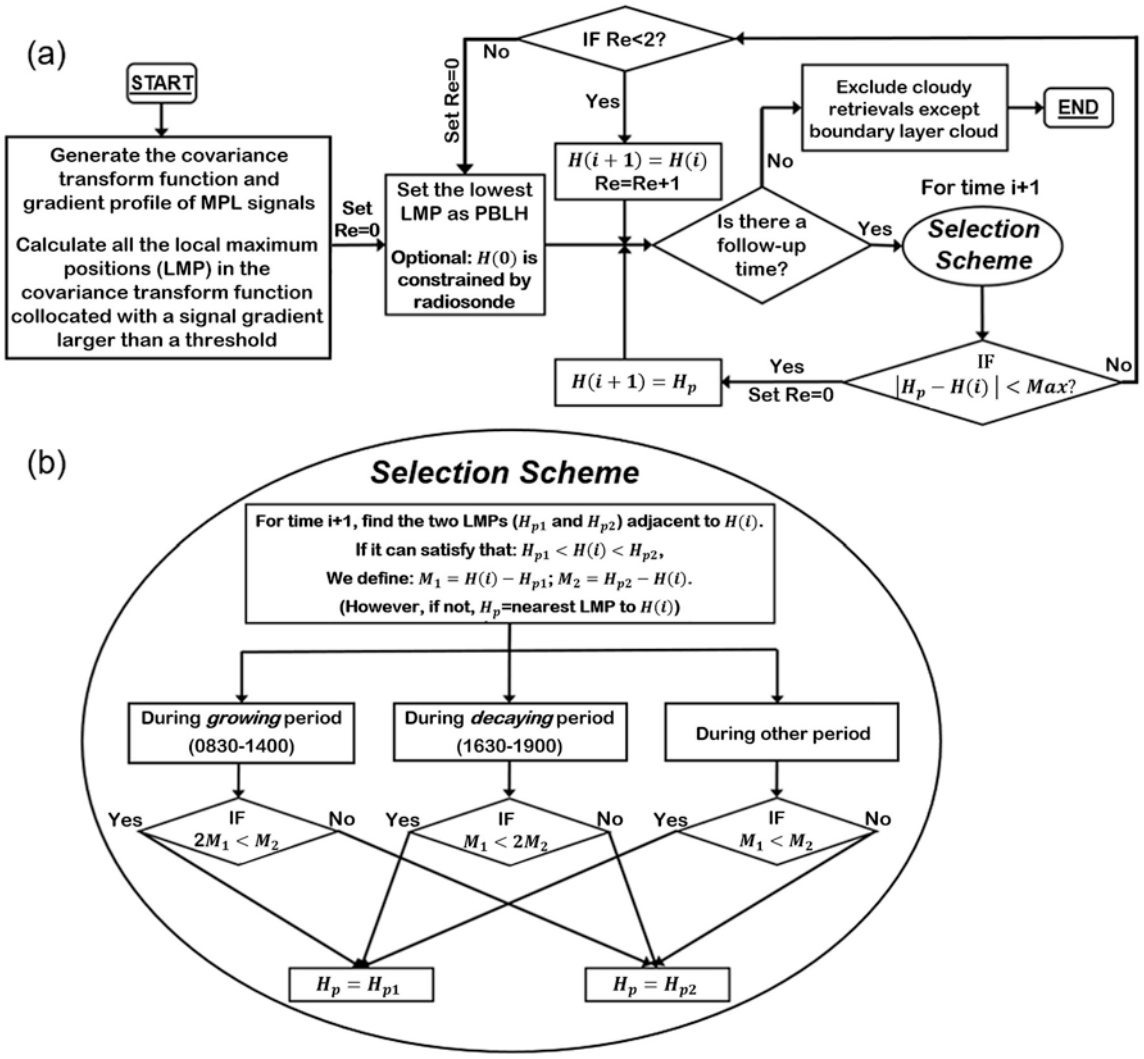

Fig. 3. (a) The overview schematic diagram of retrieving the PBLH by the DTDS. In this diagram, $H(i)$ indicates the retrieved PBLH for time i, and H_p indicates the potential PBLH position. The PBLH is retrieved at 10-min intervals. *Max* indicate the maximum variation of PBLH allowed over 10-min, and is set as 0.2 km in this study. (b) Schematic diagram of the selection scheme. The selection scheme is a process in the retrieval algorithm that describes how an appropriate local maximum position (LMP) as H_p is selected.

noise level. In particular, we estimate the shot noise (σ) induced by background light and dark currents in each profile (Welton et al., 2002; Liu et al., 2006; Whiteman et al., 2006). To exclude noise effects, the gradient signal must be larger than the shot noise. The thresholds are set between σ and 4.5 σ.

In Fig. 4, we present the correlation coefficient and RMSE values

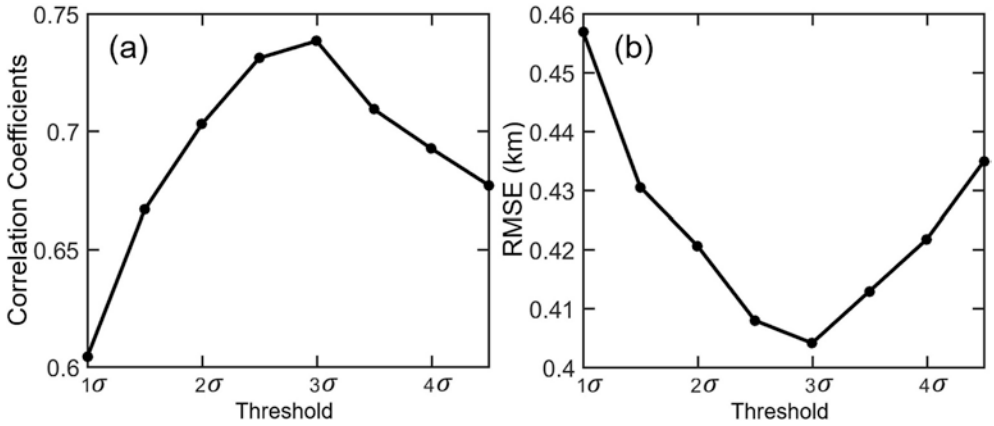

Fig. 4. Correlation coefficients and RMSE between the DTDS-derived PBLH and RS-derived PBLH under different threshold values during afternoon. The threshold value determines the algorithm LMP detection sensitivity. σ represents the shot noise induced by background light and dark current.

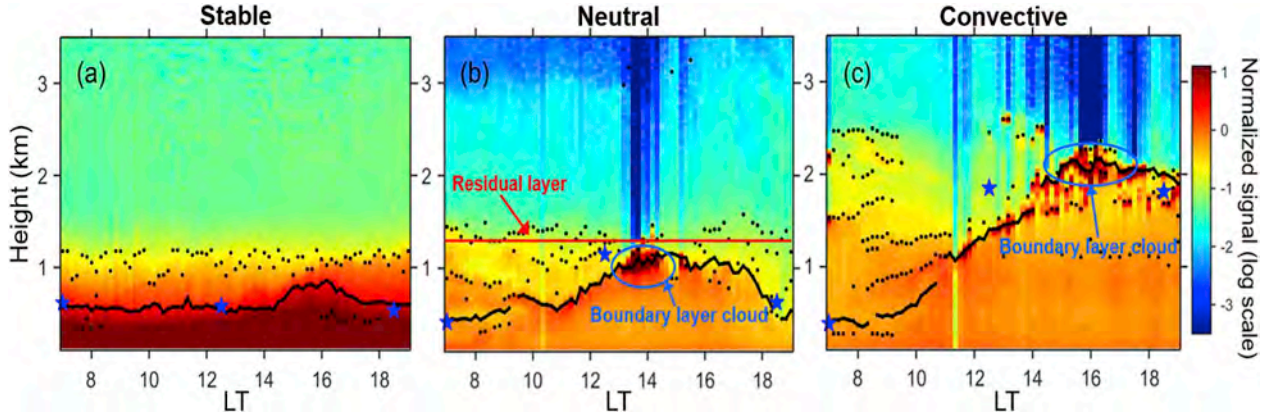

Fig. 5. Daily backscatter profiles for (a) SBL, (b) NBL, and (c) CBL cases. Backscatter is presented as a normalized signal on a log-scale, in arbitrary units. Black lines mark the PBLH retrieved from the DTDS. Black dots indicate the LMPs identified in the backscatter profiles. The blue stars indicate the PBLH as derived from RS. (For interpretation of the references to colour in this figure legend, the reader is referred to the Web version of this article.)

comparing the DTDS-derived and RS-derived PBLH based on different thresholds. For these data, we find that both the correlation coefficients and RMSE values achieve best performance when the threshold is set as 3σ. A threshold value of 3σ is thus used in the DTDS for detecting LMPs.

4. Evaluation of the DTDS

4.1. Case study of the DTDS

By using DTDS, we can continuously retrieve the daily PBLH during 0700–1900. Fig. 5 illustrates three typical cases of backscatter profiles and PBLH retrievals under different stability conditions on 25 Dec. 2014, 13 Sep. 2010, and 1 Jul. 2010, respectively. Relatively complex aerosol stratification is indicated by multiple LMPs for each profile, especially during the morning periods.

For the SBL case, clear aerosol stratification structure is shown, with little diurnal variation. Due to relatively weak convection, the PBL does not develop well during the entire day. However, there are multiple LMPs at different elevations (e.g. aerosol step signals around 0.4 km, 0.6 km, and 1 km). If we retrieve PBLH based on single profiles, the retrievals would jump between different atmospheric layers, and would not provide accurate results. With initial RS input in the morning, we coherently track the PBLH by the DTDS during the entire day, and the result agrees well with subsequent RS measurements.

For the NBL and CBL cases, the PBLH grows continuously from the initial points constrained by RS measurements, and reach maxima around 1500LT. The retrievals derived from the DTDS exclude interference from the complex aerosol structures that occur in the morning. The PBLH generally maintains its highest value during 1500–1900LT for this case. Nonetheless, the PBLH starts to decay after 1600LT for NBL. The selection scheme for the decaying period assures that our method can distinguish the actual PBL from the aerosol residual layer. Moreover, boundary layer clouds are identified for the NBL and CBL cases, and the retrieved PBLH location remains consistent with the values under cloud-free conditions.

In general, DTDS reliably tracks the true PBLH development during daytime for these three typical cases, and matches well the RS measurements. In some periods, multiple gradients are found in the lidar backscatter observations. Despite complex aerosol structure, the DTDS successfully identifies the diurnal variation of the PBLH in each case, given the initial point constraint provided by the radiosonde data.

4.2. Comparison between PBLHs derived from the DTDS and radiosonde

We further apply DTDS to the 8-year MPL dataset at the ARM SGP site, and compare the PBLH results with those from RS measurements. We prefer to use the morning RS to constrain the initial position of PBLH. However, DTDS can still perform without morning RS input. Fig. 6a–c shows comparisons between RS PBLH and PBLH derived from the DTDS without RS constraints, under different thermodynamic stability conditions during afternoon. Fig. 6d–f shows comparisons between RS PBLH and PBLH derived from DTDS with RS constraints.

Compared to the gradient and wavelet methods (Fig. 2), the correlation coefficients between PBLH derived from the DTDS and RS are higher for all PBL types, and are improved especially for the SBL cases. Although the correlation is still relatively weak for weakly convective cases, it is substantially improved relative to the gradient and wavelet methods. Moreover, compared to the RMSE for the gradient and wavelet methods, the RMSE values for the DTDS vs. RS are considerably reduced under SBL and CBL conditions. Although DTDS is valid without the morning RS input, better performance is achieved after assimilating morning RS input, especially under SBL and CBL conditions. Due to the availability of RS, we analyze the PBLH retrievals derived from the DTDS with the morning RS constraint in the following sections.

In general, the PBLH retrievals derived from DTDS are improved for all PBL types. Although the correlation coefficients are generally higher only under SBL conditions, the RMSE values are considerably reduced for both SBL and CBL in the study dataset. We supplement the validation of our method using MPL data at the MPLNET GSFC site, and compare the retrievals with RS-PBLH at nearby locations during the afternoon. DTDS also shows reasonably good performance for the GSFC site (Fig. 7). Nonetheless, due to insufficient afternoon RS data in this area, the sampling number is significantly less than at the SGP site.

4.3. Diurnal cycles

Fig. 8 presents the diurnal behavior of PBLH under SBL, NBL, and CBL conditions. As the thermodynamic condition during noontime is critical to the daily PBL development and evolution, the daily PBL types are determined from the RS measurements during 1230 LT, which generally corresponds to the most unstable period of a day. The diurnal cycles derived from the DTDS match well with RS results. Specifically, CBL is usually associated with strong solar heating of the surface, and the PBL tends to rise continuously due to upward convection around noontime, and to reach its maximum height around 1500. For cases that remain stable by midday, the PBL does not develop well during the entire day. NBL is neutrally stratified, so the potential temperature is nearly constant within the PBL, and turbulence has approximately equal intensity in all directions. The diurnal cycle for NBL is similar to CBL, but shows smaller variation.

Broadly speaking, PBLHs derived from DTDS show similar diurnal cycles with those from the gradient and wavelet methods, but with both

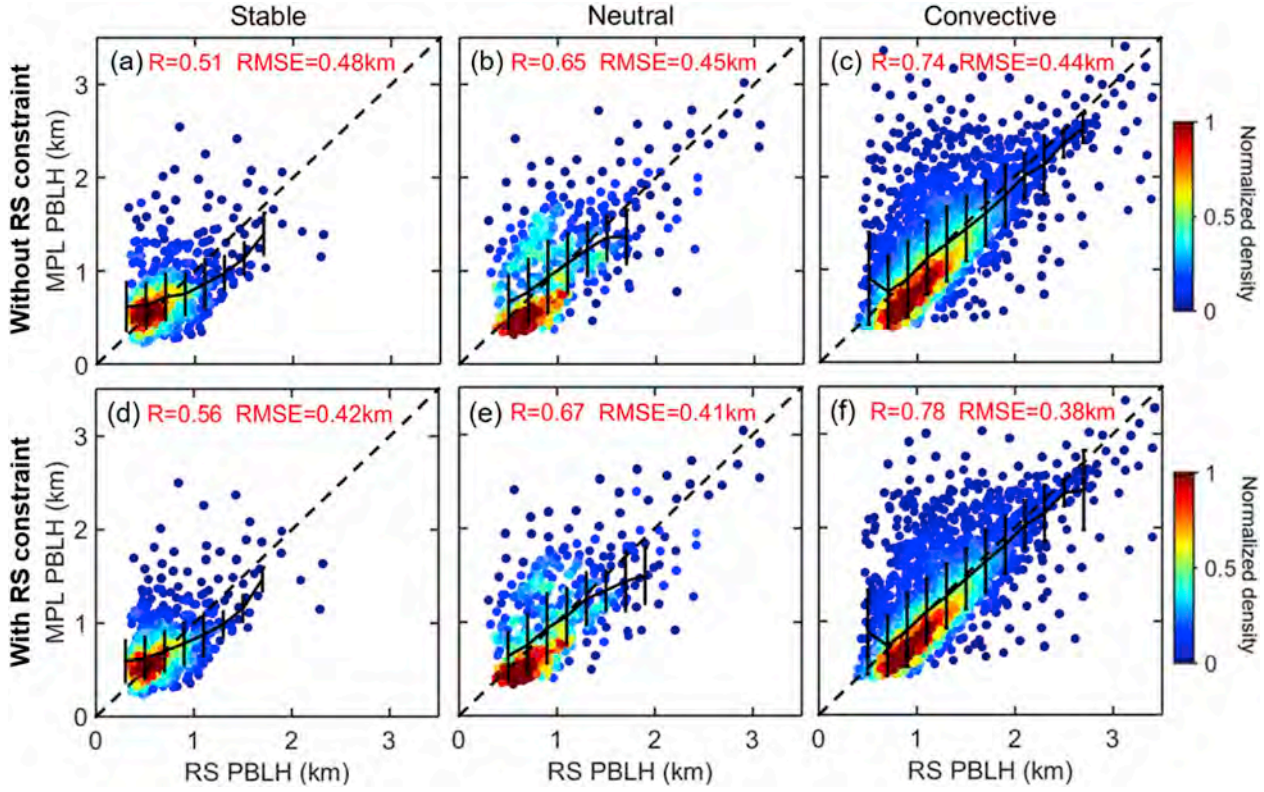

Fig. 6. Comparisons between afternoon PBLH derived from MPL and from RS under different thermodynamic stability conditions. In (a, b, c), PBLH is calculated by DTDS without the constraint of morning RS data. In (d, e, f), PBLH is calculated by DTDS with a morning RS constraint.

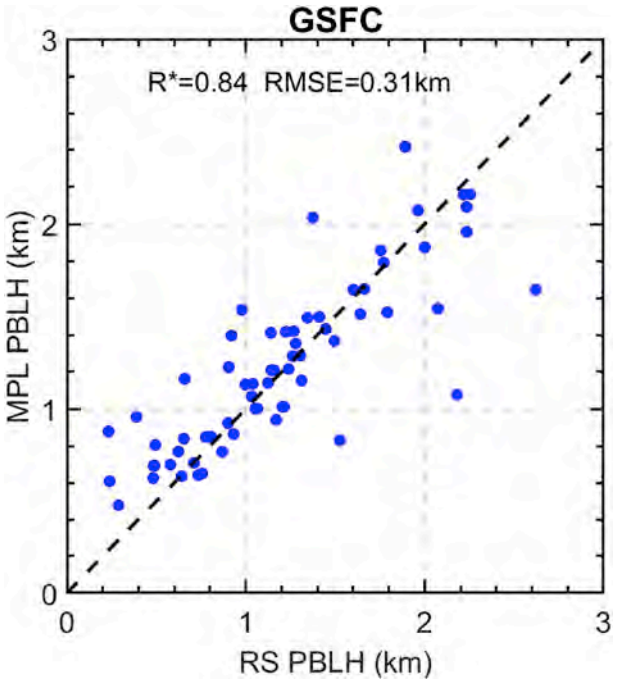

Fig. 7. Comparisons between afternoon PBLH derived from MPL and from RS at the GSFC site. PBLH is calculated by DTDS with a morning RS constraint.

smaller biases and standard deviation errors. The gradient-wavelet method tends to overestimate the PBLH for SBL, and the diurnal cycle fluctuates chaotically under these conditions, which may be caused by the algorithm assigning the PBLH to different atmospheric layers inconsistently. For CBL, the gradient-wavelet method slightly overestimates PBLH in the morning and around sunset, and slightly underestimates PBLH during midday, compared to DTDS. In term of mean values, the RS-PBLH at 1530 is significantly higher than MPL-PBLH. As the RS data are acquired at 1530 only for ~3% of total cases, sampling biases contribute significantly to the observed differences. If we only use matched cases of RS-PBLH and MPL-PBLH at 1530, the difference in the PBLH means is less than 0.1 km. For NBL, the diurnal cycles derived from the DTDS and gradient-wavelet methods generally agree well with RS and with each other.

The PBLH growth rate during transient periods is a key factor associated with boundary layer turbulence and eddies, as well as aerosol dilution (Carson, 1973; Driedonks, 1982; Martin et al., 1988). We show the distribution of PBLH growth rates during 0700–1230 LT under different thermodynamic stability conditions derived from different methods in Fig. 9. The growth rate is calculated as the average change of PBLH per hour during this period. For the majority cases, the growth rates are positive, as expected. Clearly, strong and positive buoyancy forcing under CBL conditions contributes to the large PBLH growth rate, which is near zero under SBL conditions. However, conventional lidar gradient and wavelet methods cannot capture well such phenomena; the derived PBLH growth rates are similar, and show much larger variations under different thermodynamic stability conditions. After assimilating PBLH derived from morning radiosonde data, the PBLH growth rate can be estimated by DTDS with better accuracy. The absolute bias in PBLH growth rate between RS and the wavelet/gradient methods is around 0.06 km/h, but is reduced to about 0.033 km/h between RS and the DTDS.

4.4. The impact of buoyancy forcing and aerosol loading

Because the retrieval of PBLH from lidar depends on the aerosol backscatter signal and thermodynamic stability, we further examine the absolute differences between the PBLH retrievals from lidar and RS for different aerosol loadings and stability conditions. The buoyancy (B)

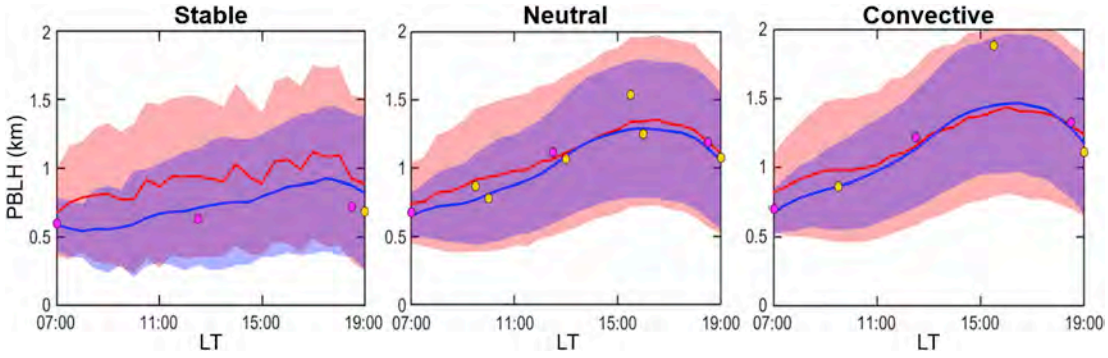

Fig. 8. Diurnal cycles of PBLH under (a) SBL, (b) NBL, and (c) CBL conditions, which are determined based on RS at 1230LT. The blue lines indicate the PBLH retrieved by the DTDS, and the red lines represent the averaged results derived from the gradient and wavelet methods. The shaded areas show the standard deviation of PBLH. Pink dots indicate the PBLH averaged from routine RS data, and yellow dots indicate the PBLH averaged from RS with limited sampling. (For interpretation of the references to colour in this figure legend, the reader is referred to the Web version of this article.)

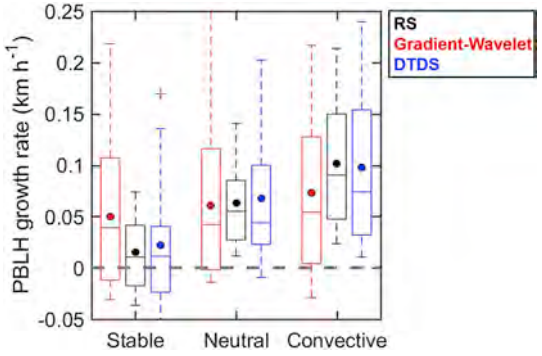

Fig. 9. Seasonal box-and-whisker plots showing 10th, 25th, 50th, 75th, and 90th percentile values of PBLH growth rate during 0700–1230 LT derived from Radiosonde (black), gradient and wavelet methods (red), and the DTDS from MPL (blue) under SBL, NBL, and CBL conditions. (For interpretation of the references to colour in this figure legend, the reader is referred to the Web version of this article.)

determines convection and can be expressed as (Wallace and Hobbs, 2006):

$$B = -g\Delta z \frac{1}{\theta}\frac{d\theta}{dz} \tag{3}$$

where z is the height of the air parcel and g is the acceleration of gravity near Earth's surface. θ is the virtual potential temperature of the environment. The lower-atmosphere buoyancy is calculated as the integral of buoyancy in the lowest 0.5 km.

We further use the near-surface aerosol extinction (at 0.2 km) derived from lidar to represent pollution levels. The method for retrieving aerosol extinction from MPL has been well demonstrated in multiple studies (e.g. Fernald, 1984; Klett, 1985). Due to the uncertainty of the extinction-to-backscatter ratio (so-called lidar ratio), we use the aerosol optical depth from multifilter rotating shadow-band radiometer (MFRSR) to calibrate the aerosol extinction profiles (Harrison et al., 1994; Sinha et al., 2013; Lee et al., 2010). Fig. 10 presents the absolute bias of PBLHs between MPL and RS for various buoyancy forcing and aerosol extinction values. Compared with the gradient-wavelet methods, the DTDS absolute bias is reduced by about 30% at various convection intensities and pollution levels. The shaded areas in Fig. 10 indicate standard deviations, which are also larger for the gradient-wavelet methods that DTDS.

The increased lower-atmosphere buoyancy can facilitate the mixing of aerosol and humidity in the PBL, and thus can considerably reduce the absolute biases between PBLH derived from RS and MPL. Meanwhile, a boomerang shape that appears in Fig. 10b indicates that relatively large differences between PBLH derived from MPL and RS happen at both low and high aerosol extinction. This phenomenon may be caused by the aerosol signal and/or thermal convection. As the detection of PBLH from lidar depends on the contrast between near-surface aerosol layers and the free troposphere, the step signal would be weak when aerosol loading is low, which could produce relatively large PBLH retrieval biases. On the other hand, high surface aerosol loading is typically associated with weak surface heating and thermal convection, producing insufficient vertical mixing of pollutants, and could therefore also cause relatively large biases for MPL retrievals.

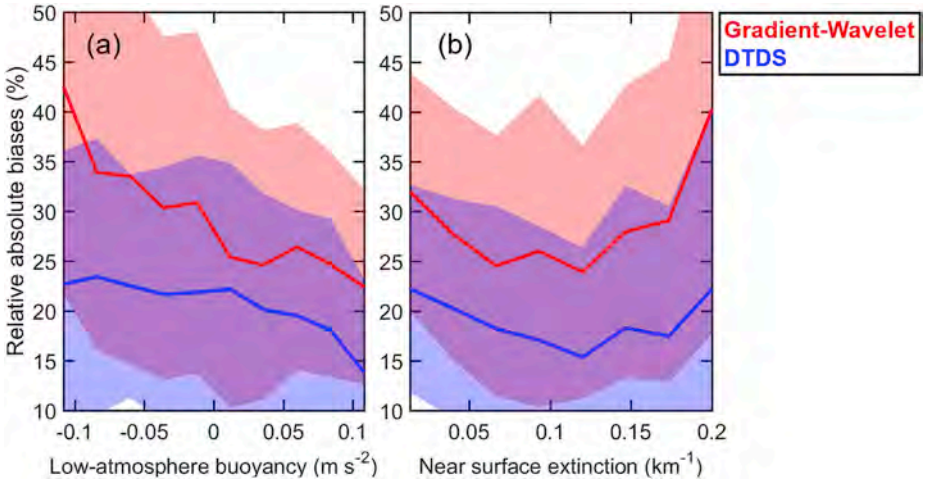

Fig. 10. Averaged relative absolute bias between afternoon PBLH derived from MPL and RS, for different (a) lower-atmosphere buoyancy and (b) near-surface aerosol extinctions. The blue line indicates the PBLH retrieved by the DTDS, and the red line represents the averaged results derived with the gradient and wavelet methods. The shaded areas indicate the standard deviations. (For interpretation of the references to colour in this figure legend, the reader is referred to the Web version of this article.)

For the gradient-wavelet methods, the relative absolute biases are strongly influenced by buoyancy forcing and aerosol loading values, and can be larger than 40% for strong downward forcing and high near-surface extinction, which are also likely to occur together. For DTDS, the contrast between different convection intensities and extinction levels is smaller, and the absolute biases are significantly reduced compared to the alternative retrieval algorithms.

5. Discussion and conclusions

In this paper, the PBL height (PBLH) retrieved from lidar is investigated systematically, under stable boundary layers (SBL), neutral boundary layers (NBL), and convective boundary layers (CBL) conditions, using an 8-year dataset of micropulse lidar (MPL) and radiosonde (RS) measurements acquired at the ARM Southern Great Plains research site. We present a DTDS algorithm aimed at accurately retrieving the PBLH under Different Thermo-Dynamic Stabilities. This method combines traditional approaches based on the observed aerosol vertical profiles with a stability-dependent model of PBLH temporal variation. Where possible, the method is initialized with early morning RS data, though this is not a strict requirement for DTDS to be applied. For the rest of the diurnal cycle, relative to the PBLH derived from radiosonde that is usually considered as ground-truth, the DTDS method performs better than the widely used gradient and wavelet methods both in terms of the PBLH magnitude and its diurnal variation, especially under SBL conditions.

The DTDS method aims to maximize the temporal continuity of the PBLH. It applies schemes specific to the growing (0830–1400 local time (LT)), decaying (1630–1900 LT) and maintenance periods for selecting successive PBLH values, based on a physical model of PBL development. Although the actual PBLH diurnal cycle is more complicated, this scheme is shown to work well for most cases studied. The PBLH derived from DTDS is likely to increase during the growing phase and decrease during the decaying phase, but the method can also identify it as declining during the period of typical growth or increasing during the period of typical decay if conditions warrant (e.g. Fig. 5a). Convective boundary layer clouds are identified to diagnose the PBLH for cloudy cases. As the PBLH is often indeterminate from MPL data alone in the morning, we tend to use the morning RS observations to constrain the initial PBLH position for subsequent retrievals, although the method is still valid without any RS data.

As a result, DTDS shows significantly improved performance in comparison to the RS-based method, with the correlation coefficient improved by up to a factor of 3–4 under SBL conditions during afternoon, when the conventional methods often fail due to the weak vertical mixing and complex aerosol stratification. RMSE is actually reduced under all conditions, though improvement is most significant under SBL and CBL conditions. The DTDS method can largely exclude interference from a residual aerosol layer and other complex aerosol structures.

The PBLH derived from lidar is widely used to investigate air quality issues and thermodynamic processes in the PBL (e.g. Beniston et al., 1990; Davies et al., 2007; Geiss et al., 2017; Su et al., 2018; Tang et al., 2015). Although the lidar retrievals exhibit satisfactory overall performance, the accuracy of lidar retrievals can vary considerably under different stability conditions and aerosol levels, and thus, may cause uncertainties in these studies. This problem is not completely solved, but our method gives some insight into this issue by reducing biases under various stability conditions and aerosol loadings.

Stable conditions are associated with downward forcing in the lower atmosphere, and they exert important constraints on severe pollution episodes. Being able to detect the PBLH under such conditions would help understand and model the development of air pollution episodes, especially in the morning before the PBL is fully developed. The method is also valuable for investigating PBL-aerosol interaction mechanisms under various meteorological and thermodynamic stability conditions, which remains an outstanding problem in studies concerning atmospheric environment (Li et al., 2017b). The PBLH derived using the DTDS approach may also be beneficial for pollution control management, as it helps improve understanding of aerosol dispersion.

Acknowledgements

We acknowledge the provision of radiosonde and MPL data by the U.S. Department of Energy's ARM program (https://www.archive.arm.gov/discovery). We thank Dr. E. J. Welton and his team for their efforts in establishing and maintaining the GSFC site. We extend sincerest thanks to the MPLNET for their datasets. This work is supported in part by grants from the National Science Foundation (AGS1837811), the U.S. Department if Energy (DE-SC0018996), and NASA (NNX16AN61G). The contributions of R. Kahn are supported in part by NASA's Climate and Radiation Research and Analysis Program under H. Maring, and NASA's Atmospheric Composition Modeling and Analysis Program under R. Eckman.

References

Amiridis, V., Melas, D., Balis, D.S., Papayannis, A., Founda, D., Katragkou, E., Giannakaki, E., Mamouri, R.E., Gerasopoulos, E., Zerefos, C., 2007. Aerosol lidar observations and model calculations of the planetary boundary layer evolution over Greece, during the march 2006 total solar eclipse. Atmos. Chem. Phys. 7, 6181–6189.

Angevine, W.M., White, A.B., Avery, S.K., 1994. Boundary-layer depth and entrainment zone characterization with a boundary-layer profiler. Boundary-Layer Meteorol. 68, 375–385.

Baars, H., Ansmann, A., Engelmann, R., Althausen, D., 2008. Continuous monitoring of the boundary-layer top with lidar. Atmos. Chem. Phys. 8, 7281–7296.

Beniston, M., Wolf, J.P., Benistonrebetez, M., Kolsch, H.J., Rairoux, P., Woste, L., 1990. Use of lidar measurements and numerical-models in air-pollution research. J. Geophysics. Res. Atmos. 95, 9879–9894.

Boers, R., Eloranta, E.W., Coulter, R.L., 1984. Lidar observations of mixed layer dynamics - tests of parameterized entrainment models of mixed layer growth-rate. J. Clim. Appl. Meteorol. 23, 247–266.

Bravo-Aranda, J.A., Moreira, G.D., Navas-Guzman, F., Granados-Munoz, M.J., Guerrero-Rascado, J.L., Pozo-Vazquez, D., Arbizu-Barrena, C., Reyes, F.J.O., Mallet, M., Arboledas, L.A., 2017. A new methodology for PBL height estimations based on lidar depolarization measurements: analysis and comparison against MWR and WRF model-based results. Atmos. Chem. Phys. 17, 6839–6851.

Brooks, I.M., 2003. Finding boundary layer top: application of a wavelet covariance transform to lidar backscatter profiles. J. Atmos. Ocean. Technol. 20, 1092–1105.

Campbell, J.R., Hlavka, D.L., Welton, E.J., Flynn, C.J., Turner, D.D., Spinhirne, J.D., Scott, V.S., Hwang, I.H., 2002. Full-time, eye-safe cloud and aerosol lidar observation at atmospheric radiation measurement program sites: instruments and data processing. J. Atmos. Ocean. Technol. 19, 431–442.

Campbell, J.R., Welton, E.J., Spinhirne, J.D., Ji, Q., Tsay, S.C., Piketh, S.J., Barenbrug, M., Holben, B.N., 2003. Micropulse lidar observations of tropospheric aerosols over northeastern South Africa during the ARREX and SAFARI 2000 dry season experiments. J. Geophysics. Res. Atmos. *108*.

Carson, D.J., 1973. The development of a dry inversion-capped convectively unstable boundary layer. Q. J. R. Meteorol. Soc. 99, 450–467.

Caughey, S.J., Palmer, S.G., 1979. Some aspects of turbulence structure through the depth of the convective boundary-layer. Q. J. R. Meteorol. Soc. 105, 811–827.

Caughey, S.J., 1984. Observed characteristics of the atmospheric boundary layer. In: Atmospheric Turbulence and Air Pollution Modelling. Springer, Dordrecht, pp. 107–158.

Chu, Y., Li, J., Li, C., Tan, W., Su, T., Li, J., 2019. Seasonal and diurnal variability of planetary boundary layer height in Beijing: intercomparison between MPL and WRF results. Atmos. Res. 227, 1–13.

Crawford, J.H., Pickering, K.E., 2014. DISCOVER-AQ: advancing strategies for air quality observations in the next decade. Environ. Manag. 4–7.

Cohn, S.A., Angevine, W.M., 2000. Boundary layer height and entrainment zone thickness measured by lidars and wind-profiling radars. J. Appl. Meteorol. 39, 1233–1247.

Compton, J.C., Delgado, R., Berkoff, T.A., Hoff, R.M., 2013. Determination of planetary boundary layer height on short spatial and temporal scales: a demonstration of the covariance wavelet transform in ground-based wind profiler and lidar measurements. J. Atmos. Ocean. Technol. 30, 1566–1575.

Davies, F., Middleton, D.R., Bozier, K.E., 2007. Urban air pollution modelling and measurements of boundary layer height. Atmos. Environ. 41, 4040–4049.

Davis, K.J., Gamage, N., Hagelberg, C.R., Kiemle, C., Lenschow, D.H., Sullivan, P.P., 2000. An objective method for deriving atmospheric structure from airborne lidar observations. J. Atmos. Ocean. Technol. 17, 1455–1468.

Driedonks, A.G.M., 1982. Models and observations of the growth of the atmospheric boundary-layer. Boundary-Layer Meteorol. 23, 283–306.

Dupont, J.C., Haeffelin, M., Morille, Y., Comstock, J.M., Flynn, C., Long, C.N., Sivaraman, C., Newson, R.K., 2011. Cloud properties derived from two lidars over the ARM SGP site. Geophys. Res. Lett. *38*.

Emanuel, K.A., 1994. Atmospheric Convection. Oxford University Press on Demand.
Eresmaa, N., Karppinen, A., Joffre, S.M., Rasanen, J., Talvitie, H., 2006. Mixing height determination by ceilometer. Atmos. Chem. Phys. 6, 1485–1493.
Fernald, F.G., 1984. Analysis of atmospheric lidar observations: some comments. Appl. Opt. 23 652e653.
Flamant, C., Pelon, J., Flamant, P.H., Durand, P., 1997. Lidar determination of the entrainment zone thickness at the top of the unstable marine atmospheric boundary layer. Boundary-Layer Meteorol. 83, 247–284.
Gamage, N., Hagelberg, C., 1993. Detection and analysis of microfronts and associated coherent events using localized transforms. J. Atmos. Sci. 50, 750–756.
Gan, C.M., Wu, Y.H., Madhavan, B.L., Gross, B., Moshary, F., 2011. Application of active optical sensors to probe the vertical structure of the urban boundary layer and assess anomalies in air quality model PM2.5 forecasts. Atmos. Environ. 45, 6613–6621.
Garratt, J.R., 1994. The atmospheric boundary-layer - review. Earth Sci. Rev. 37, 89–134.
Geiss, A., Wiegner, M., Bonn, B., Schafer, K., Forkel, R., von Schneidemesser, E., Munkel, C., Chan, K.L., Nothard, R., 2017. Mixing layer height as an indicator for urban air quality? Atmospheric Measurement Techniques 10, 2969–2988.
Guo, J.P., Miao, Y.C., Zhang, Y., Liu, H., Li, Z.Q., Zhang, W.C., He, J., Lou, M.Y., Yan, Y., Bian, L.G., Zhai, P., 2016. The climatology of planetary boundary layer height in China derived from radiosonde and reanalysis data. Atmos. Chem. Phys. 16, 13309–13319.
Guo, J.P., Su, T.N., Li, Z.Q., Miao, Y.C., Li, J., Liu, H., Xu, H., Cribb, M., Zhai, P.M., 2017. Declining frequency of summertime local-scale precipitation over eastern China from 1970 to 2010 and its potential link to aerosols. Geophys. Res. Lett. 44, 5700–5708.
Haeffelin, M., Angelini, F., Morille, Y., Martucci, G., Frey, S., Gobbi, G.P., Lolli, S., O'Dowd, C.D., Sauvage, L., Xueref-Remy, I., Wastine, B., Feist, D.G., 2012. Evaluation of mixing-height retrievals from automatic profiling lidars and ceilometers in view of future integrated networks in europe. Boundary-Layer Meteorol. 143, 49–75.
Hageli, P., Steyn, D.G., Strawbridge, K.B., 2000. Spatial and temporal variability of mixed-layer depth and entrainment zone thickness. Boundary-Layer Meteorol. 97, 47–71.
Harrison, L., Michalsky, J., Berndt, J., 1994. Automated multifilter rotating shadow-band radiometer - an instrument for optical depth and radiation measurements. Appl. Optic. 33, 5118–5125.
He, Q.S., Mao, J.T., Chen, J.Y., Hu, Y.Y., 2006. Observational and modeling studies of urban atmospheric boundary-layer height and its evolution mechanisms. Atmos. Environ. 40, 1064–1077.
Holtslag, A.A., Nieuwstadt, F.T., 1986. Scaling the atmospheric boundary layer. Boundary-Layer Meteorol. 36 (1–2), 201–209.
Hooper, W.P., Eloranta, E.W., 1986. Lidar measurements of wind in the planetary boundary-layer - the method, accuracy and results from joint measurements with radiosonde and kytoon. J. Clim. Appl. Meteorol. 25, 990–1001.
Kaimal, J.C., Finnigan, J.J., 1994. Atmospheric Boundary Layer Flows: Their Structure and Measurement. Oxford university press.
Klett, J.D., 1985. Lidar inversion with variable backscatter extinction ratios. Appl. Optic. 24, 1638–1643.
Lee, K.H., Li, Z.Q., Cribb, M.C., Liu, J.J., Wang, L., Zheng, Y.F., Xia, X.G., Chen, H.B., Li, B., 2010. Aerosol optical depth measurements in eastern China and a new calibration method. J. Geophysics. Res. Atmos. *115*.
Lewis, J.R., Welton, E.J., Molod, A.M., Joseph, E., 2013. Improved boundary layer depth retrievals from MPLNET. J. Geophys. Res.: Atmosphere 118 (17), 9870–9879.
Li, H., Yang, Y., Hu, X.M., Huang, Z.W., Wang, G.Y., Zhang, B.D., Zhang, T.J., 2017a. Evaluation of retrieval methods of daytime convective boundary layer height based on lidar data. J. Geophysics. Res. Atmos. 122, 4578–4593.
Li, Z.Q., Guo, J.P., Ding, A.J., Liao, H., Liu, J.J., Sun, Y.L., Wang, T.J., Xue, H.W., Zhang, H.S., Zhu, B., 2017b. Aerosol and boundary-layer interactions and impact on air quality. National Science Review 4, 810–833.
Lilly, D.K., 1968. Models of cloud-topped mixed layers under a strong inversion. Q. J. R. Meteorol. Soc. 94, 292–&.
Liu, B.M., Ma, Y.Y., Gong, W., Jian, Y., Ming, Z., 2018. Two-wavelength Lidar inversion algorithm for determining planetary boundary layer height. J. Quant. Spectrosc. Radiat. Transfer 206, 117–124.
Liu, S.Y., Liang, X.Z., 2010. Observed diurnal cycle climatology of planetary boundary layer height. J. Clim. 23, 5790–5809.
Liu, Z.Y., Hunt, W., Vaughan, M., Hostetler, C., McGill, M., Powell, K., Winker, D., Hu, Y.X., 2006. Estimating random errors due to shot noise in backscatter lidar observations. Appl. Optic. 45, 4437–4447.
Lou, M., Guo, J., Wang, L., Xu, H., Chen, D., Miao, Y., et al., 2019. On the relationship between aerosol and boundary layer height in summer in China under different thermodynamic conditions. Earth and Space Science (in press).
Luo, T., Yuan, R., Wang, Z., 2014. Lidar-based remote sensing of atmospheric boundary layer height over land and ocean. Atmospheric Measurement Techniques 7, 173–182.
Mahrt, L., 1999. Stratified atmospheric boundary layers. Boundary-Layer Meteorol. 90 (3), 375–396.
Martin, C.L., Fitzjarrald, D., Garstang, M., Oliveira, A.P., Greco, S., Browell, E., 1988. Structure and growth of the mixing layer over the amazonian rain-forest. J. Geophysics. Res. Atmos. 93, 1361–1375.
Matsui, T., Masunaga, H., Pielke, R.A., Tao, W.K., 2004. Impact of aerosols and atmospheric thermodynamics on cloud properties within the climate system. Geophys. Res. Lett. *31*.
Medeiros, B., Hall, A., Stevens, B., 2005. What controls the mean depth of the PBL? J. Clim. 18, 3157–3172.
Melfi, S.H., Spinhirne, J.D., Chou, S.H., Palm, S.P., 1985. Lidar observations of vertically organized convection in the planetary boundary-layer over the ocean. J. Clim. Appl. Meteorol. 24, 806–821.
Menut, L., Flamant, C., Pelon, J., Flamant, P.H., 1999. Urban boundary-layer height determination from lidar measurements over the Paris area. Appl. Optic. 38, 945–954.
Miao, Y.C., Guo, J.P., Liu, S.H., Wei, W., Zhang, G., Lin, Y.L., Zhai, P.M., 2018. The climatology of low-level jet in beijing and guangzhou, China. J. Geophysics. Res. Atmos. 123, 2816–2830.
Monks, P.S., Granier, C., Fuzzi, S., Stohl, A., Williams, M.L., Akimoto, H., Amann, M., Baklanov, A., Baltensperger, U., Bey, I., Blake, N., Blake, R.S., Carslaw, K., Cooper, O.R., Dentener, F., Fowler, D., Fragkou, E., Frost, G.J., Generoso, S., Ginoux, P., Grewe, V., Guenther, A., Hansson, H.C., Henne, S., Hjorth, J., Hofzumahaus, A., Huntrieser, H., Isaksen, I.S.A., Jenkin, M.E., Kaiser, J., Kanakidou, M., Klimont, Z., Kulmala, M., Laj, P., Lawrence, M.G., Lee, J.D., Liousse, C., Maione, M., McFiggans, G., Metzger, A., Mieville, A., Moussiopoulos, N., Orlando, J.J., O'Dowd, C.D., Palmer, P.I., Parrish, D.D., Petzold, A., Platt, U., Poschl, U., Prevot, A.S.H., Reeves, C.E., Reimann, S., Rudich, Y., Sellegri, K., Steinbrecher, R., Simpson, D., ten Brink, H., Theloke, J., van der Werf, G.R., Vautard, R., Vestreng, V., Vlachokostas, C., von Glasow, R., 2009. Atmospheric composition change - global and regional air quality. Atmos. Environ. 43, 5268–5350.
Morille, Y., Haeffelin, M., Drobinski, P., Pelon, J., 2007. STRAT: an automated algorithm to retrieve the vertical structure of the atmosphere from single-channel lidar data. J. Atmos. Ocean. Technol. 24, 761–775.
Nieuwstadt, F.T.M., 1984. The turbulent structure of the stable, nocturnal boundary-layer. J. Atmos. Sci. 41, 2202–2216.
Park, O.H., Seo, S.J., Lee, S.H., 2001. Laboratory simulation of vertical plume dispersion within a convective boundary layer - research note. Boundary-Layer Meteorol. 99, 159–169.
Platt, C.M., Young, S.A., Carswell, A.I., Pal, S.R., Mccormick, M.P., Winker, D.M., Delguasta, M., Stefanutti, L., Eberhard, W.L., Hardesty, M., Flamant, P.H., Valentin, R., Forgan, B., Gimmestad, G.G., Jager, H., Khmelevtsov, S.S., Kolev, I., Kaprieolev, B., Lu, D.R., Sassen, K., Shamanaev, V.S., Uchino, O., Mizuno, Y., Wandinger, U., Weitkamp, C., Ansmann, A., Wooldridge, C., 1994. The experimental cloud lidar pilot-study (eclips) for cloud-radiation research. Bull. Am. Meteorol. Soc. 75, 1635–1654.
Poltera, Y., Martucci, G., Coen, M.C., Hervo, M., Emmenegger, L., Henne, S., Brunner, D., Haefele, A., 2017. PathfinderTURB: an automatic boundary layer algorithm. Development, validation and application to study the impact on in situ measurements at the Jungfraujoch. Atmos. Chem. Phys. 17, 10051–10070.
Poulos, G.S., Blumen, W., Fritts, D.C., Lundquist, J.K., Sun, J., Burns, S.P., Nappo, C., Banta, R., Newsom, R., Cuxart, J., Terradellas, E., Balsley, B., Jensen, M., 2002. CASES-99: a comprehensive investigation of the stable nocturnal boundary layer. Bull. Am. Meteorol. Soc. 83, 555–581.
Sawyer, V., Li, Z.Q., 2013. Detection, variations and intercomparison of the planetary boundary layer depth from radiosonde, lidar and infrared spectrometer. Atmos. Environ. 79, 518–528.
Seibert, P., Beyrich, F., Gryning, S.E., Joffre, S., Rasmussen, A., Tercier, P., 2000. Review and intercomparison of operational methods for the determination of the mixing height. Atmos. Environ. 34, 1001–1027.
Seidel, D.J., Ao, C.O., Li, K., 2010. Estimating climatological planetary boundary layer heights from radiosonde observations: comparison of methods and uncertainty analysis. J. Geophysics. Res. Atmos. *115*.
Sicard, M., Perez, C., Rocadenbosch, F., Baldasano, J.M., Garcia-Vizcaino, D., 2006. Mixed-layer depth determination in the Barcelona coastal area from regular lidar measurements: methods, results and limitations. Boundary-Layer Meteorol. 119, 135–157.
Sinha, P.R., Manchanda, R.K., Kaskaoutis, D.G., Kumar, Y.B., Sreenivasan, S., 2013. Seasonal variation of surface and vertical profile of aerosol properties over a tropical urban station Hyderabad, India: vertical aerosol characteristics. J. Geophys. Res. Atmos. 118, 749e768.
Steyn, D.G., Baldi, M., Hoff, R.M., 1999. The detection of mixed layer depth and entrainment zone thickness from lidar backscatter profiles. J. Atmos. Ocean. Technol. 16, 953–959.
Stull, R.B., 1988. An Introduction to Boundary Layer Meteorology. Springer Netherlands, Dordrecht.
Su, T.N., Li, J., Li, C.C., Lau, A.K.H., Yang, D.W., Shen, C.Y., 2017a. An intercomparison of AOD-converted PM2.5 concentrations using different approaches for estimating aerosol vertical distribution. Atmos. Environ. 166, 531–542.
Su, T.N., Li, J., Li, C.C., Xiang, P.Z., Lau, A.K.H., Guo, J.P., Yang, D.W., Miao, Y.C., 2017b. An intercomparison of long-term planetary boundary layer heights retrieved from CALIPSO, ground-based lidar, and radiosonde measurements over Hong Kong. J. Geophysics. Res. Atmos. 122, 3929–3943.
Su, T.N., Li, Z.Q., Kahn, R., 2018. Relationships between the planetary boundary layer height and surface pollutants derived from lidar observations over China: regional pattern and influencing factors. Atmos. Chem. Phys. 18, 15921–15935.
Summa, D., Di Girolamo, P., Stelitano, D., Cacciani, M., 2013. Characterization of the planetary boundary layer height and structure by Raman lidar: comparison of different approaches. Atmospheric Measurement Techniques 6, 3515–3525.
Tang, G., Zhu, X., Hu, B., Xin, J., Wang, L., Munkel, C., Mao, G., Wang, Y., 2015. Impact of emission controls on air quality in Beijing during APEC 2014: lidar ceilometer observations. Atmos. Chem. Phys. 15, 12667–12680.
Tokinaga, H., Tanimoto, Y., Nonaka, M., Taguchi, B., Fukamachi, T., Xie, S.P., Nakamura, H., Watanabe, T., Yasuda, I., 2006. Atmospheric sounding over the winter Kuroshio Extension: effect of surface stability on atmospheric boundary layer structure. Geophys. Res. Lett. *33*.
Tucker, S.C., Brewer, W.A., Banta, R.M., Senff, C.J., Sandberg, S.P., Law, D.C., Weickmann, A.M., Hardesty, R.M., 2009. Doppler lidar estimation of mixing height using turbulence, shear, and aerosol profiles. J. Atmos. Ocean. Technol. 26, 673–688.
Wallace, J.M., Hobbs, P.V., 2006. Atmospheric Science: an Introductory Survey. Elsevier.

Wang, Z., Sassen, K., 2001. Cloud type and macrophysical property retrieval using multiple remote sensors. J. Appl. Meteorol. 40 (10), 1665–1682.
Welton, E.J., Voss, K.J., Gordon, H.R., Maring, H., Smirnov, A., Holben, B., et al., 2000. Ground-based lidar measurements of aerosols during ACE-2: instrument description, results, and comparisons with other ground-based and airborne measurements. Tellus B 52 (2), 636–651.
Welton, E.J., Campbell, J.R., Spinhirne, J.D., Scott, V.S., 2001. In: In: Singh, U.N., Itabe, T., Sugimoto, N. (Eds.), Globalmonitoring of Clouds and Aerosols Using a Network of Micro-pulse Lidarsystems, inLidar Remote Sensing for Industry and Environmental Mon-itoring, vol. 4153. Proc. SPIE, Sendai, Japan, pp. 151–158.
Welton, E.J., Campbell, J.R., 2002. Micropulse lidar signals: uncertainty analysis. J. Atmos. Ocean. Technol. 19, 2089–2094.
Whiteman, D.N., Demoz, B., Di Girolamo, P., Comer, J., Veselovskii, I., Evans, K., Wang, Z., Cadirola, M., Rush, K., Schwemmer, G., Gentry, B., Melfi, S.H., Mielke, B., Venable, D., Van Hove, T., 2006. Raman lidar measurements during the International H2O Project. Part I: instrumentation and analysis techniques. J. Atmos. Ocean. Technol. 23, 157–169.
Yan, H.R., Li, Z.Q., Huang, J.P., Cribb, M., Liu, J.J., 2014. Long-term aerosol-mediated changes in cloud radiative forcing of deep clouds at the top and bottom of the atmosphere over the Southern Great Plains. Atmos. Chem. Phys. 14, 7113–7124.
Yang, D.W., Li, C.C., Lau, A.K.H., Li, Y., 2013. Long-term measurement of daytime atmospheric mixing layer height over Hong Kong. J. Geophysics. Res. Atmos. 118, 2422–2433.
Yang, T., Wang, Z.F., Zhang, W., Gbaguidi, A., Sugimoto, N., Wang, X.Q., Matsui, I., Sun, Y.L., 2017. Technical note: boundary layer height determination from lidar for improving air pollution episode modeling: development of new algorithm and evaluation. Atmos. Chem. Phys. 17, 6215–6225.
Zhao, C., Wang, Y., Wang, Q., Li, Z., Wang, Z., Liu, D., 2014. A new cloud and aerosol layer detection method based on micropulse lidar measurements. J. Geophys. Res.: Atmosphere 119 (11), 6788–6802.
Zhang, W., Guo, J., Miao, Y., Liu, H., Zhang, Y., Li, Z., Zhai, P., 2016. Planetary boundary layer height from CALIOP compared to radiosonde over China. Atmos. Chem. Phys. 16 (15), 9951–9963.
Zhang, W.C., Guo, J.P., Miao, Y.C., Liu, H., Song, Y., Fang, Z., He, J., Lou, M.Y., Yan, Y., Li, Y., Zhai, P.M., 2018. On the summertime planetary boundary layer with different thermodynamic stability in China: a radiosonde perspective. J. Clim. 31, 1451–1465.